

1 Assessing the role of clay and salts on the origin of MARSIS basal bright 2 reflections

3
4
5 Elisabetta Mattei¹, Elena Pettinelli^{1*}, Sebastian Emanuel Lauro¹, David E. Stillman², Barbara
6 Cosciotti¹, Lucia Marinangeli³, Anna Chiara Tangari³, Francesco Soldovieri⁴, Roberto Orosei⁵ and
7 Graziella Caprarelli⁶

8
9
10 Corresponding author: elena.pettinelli@uniroma3.it

11 Affiliations:

12
13
14 ¹ Dipartimento di Matematica e Fisica, Università degli studi Roma Tre, Rome, Italy

15 ² Department of Space Studies, Southwest Research Institute, Boulder, USA

16 ³ Dipartimento di Scienze Psicologiche, della Salute e del Territorio, Università degli studi “G.
17 D’Annunzio” Chieti – Pescara, Chieti, Italy

18 ⁴ Istituto per il Rilevamento Elettromagnetico dell’Ambiente, Consiglio Nazionale delle Ricerche,
19 Naples, Italy

20 ⁵ Istituto di Radioastronomia (IRA), Istituto Nazionale di Astrofisica (INAF), Bologna, Italy

21 ⁶ Centre for Astrophysics, Institute for Advanced Engineering and Space Sciences, University of
22 Southern Queensland, Toowomba, Australia

23 24 25 26 **Highlights**

- 27 • Bright basal reflections have been detected by MARSIS at Ultimi Scopuli, Mars
 - 28 • High permittivity contrast between the ice and the basal material is required
 - 29 • Wet sediments or ponded water have been suggested as the cause of such reflections
 - 30 • Hydrous minerals and salts are considered as possible alternative to basal water
 - 31 • Only brines can generate such high dielectric contrast at low basal temperature
- 32
33

35 Abstract

36 Anomalous bright basal reflections detected by MARSIS at Ultimi Scopuli have been interpreted
37 to indicate the presence of water-saturated materials or ponded liquid water at the base of the South
38 Polar Layered Deposits (SPLD). Because conventional models assume basal temperatures ($\leq 200\text{K}$)
39 much lower than the melting point of water, this interpretation has been questioned and other
40 explanations for the source of the bright basal reflections have been proposed, involving clay,
41 hydrated salts, and saline ices. Combining previous published data, simulations, and new laboratory
42 measurements, we demonstrate that the dielectric properties of these materials do not generate
43 strong basal reflections at MARSIS frequencies and Martian temperatures. Plausible candidates
44 remain perchlorates and chlorides brines that exhibit a strong dielectric response at much lower
45 temperatures than other materials. This explanation might require that metastability could be
46 maintained for a long period of time on a geological scale.

47

48 **Keywords:** MARSIS, bright radar reflections, permittivity, clay, salts, brines

49

50

51 1. Introduction

52 In the last fifty years, terrestrial Radar Echo Sounding (RES) technique has played a fundamental
53 role in detecting subglacial liquid water and understanding the hydrological processes beneath
54 Antarctica and Greenland ice sheets (Siegert, 2018). Planetary radar sounders could now play a
55 similar role for Mars. Recently, MARSIS (Mars Advanced Radar for Subsurface and Ionosphere
56 Sounding), onboard Mars Express spacecraft, detected bright reflections from the base of the
57 Martian South Polar Layered Deposits (SPLD) at Ultimi Scopuli (Orosei et al., 2018; Lauro et al.,
58 2021). Such reflections have characteristics comparable to those acquired by terrestrial RES above
59 subglacial water ponded areas (Lauro et al., 2021), and were therefore interpreted as caused by
60 (partially) water-saturated materials and/or layers of liquid water. Given the low temperatures
61 commonly inferred at the base of the SPLD (of the order of 200 K or lower) (Wieczorek, 2008;
62 Plesa et al., 2018; Sori and Bramson, 2019), liquid water can only exist as aqueous solutions of
63 salts known to strongly depress the freezing point of water, such as perchlorates, chlorates and
64 chlorides [e.g., Chevrier et al. (2009); Toner, and Catling (2018); Primm et al. (2020); Stillman et
65 al. (2021)]. Briny waters are common in terrestrial glacial environments and are considered to be

66 some of the brightest englacial or subglacial reflectors detectable with radar sounders [e.g., Nobes
67 et al. (2005); Grima et al. (2016); Rutishauser et al. (2018)].

68 Other subglacial water-saturated sediments, especially clay, could however also produce a strong
69 radar response [e.g., Tulaczyk and Foley (2020)]. On Mars, clay and other hydrous mineral bearing
70 deposits have been identified in many outcrops both remotely by OMEGA (Observatoire pour la
71 Minéralogie, l'Eau, les Glaces, et l'Activité) (Bibring et al., 2006) onboard Mars Express and
72 CRISM (Compact Reconnaissance Imaging Spectrometer for Mars) onboard Mars Reconnaissance
73 Orbiter (Murchie et al., 2007), and in situ by the NASA Spirit and Curiosity rovers at the Gusev
74 and Gale craters landing sites [e.g., Clark et al. (2007); Bristow et al. (2018); Rampe et al. (2020a)].
75 Though no clear evidence of clay and salt outcrops in the terrains surrounding the SPLD has been
76 reported so far, their presence in the sediments at the base of the ice cannot be positively ruled out.
77 To assess the possibility that clay-rich sediments could produce basal reflections as strong as those
78 detected by MARSIS [e.g., Bierson et al. (2021); Smith et al. (2021)], we performed dielectric
79 laboratory measurements on Martian clay analogs. Here we compare our results to previously
80 published work on the dielectric properties of clay and salts at Martian temperatures, and to data
81 obtained from MARSIS observations at Ultimi Scopuli. We also discuss the role of specific briny
82 materials in the generation of bright basal reflections.

83

84 **2. Salts and clays on Mars**

85 Hydrous minerals and salts are largely present on Mars: they have been found in samples of Martian
86 meteorites (Gooding and Muenow, 1986; Treiman et al., 1993; McSween, 1994; Leshin and
87 Vicenzi, 2006; Muttik et al., 2014; Kounaves et al., 2014), and detected through orbital and lander
88 observations (Murchie et al., 2009; Ehlmann and Edwards, 2014). The formation of hydrous
89 minerals has been explained by a variety of processes, including late volcanic/hydrothermal
90 activity, low-grade metamorphism, deposition by migrating groundwaters, surface deposition in
91 fluvio-lacustrine or playa environments, adsorption of atmospheric water. Significant amounts of
92 hydrous minerals have not been detected at high latitudes, where they are probably masked by a
93 thin latitude dependent sedimentary layer (Mustard et al., 2001), and by polar processes. About
94 70% of phyllosilicates detections on Mars are of Fe/Mg smectites (nontronite, saponite) and
95 chlorite, followed in abundance by Al-smectites (montmorillonite, beidellite) (Ehlmann et al.,
96 2011). Quantitative analysis based on Curiosity rover measurements indicate an amount of clay
97 minerals ranging between 3 and 28% in fluvio-lacustrine sediments of Gale Crater mainly
98 containing smectite (Bristow et al., 2018; Rampe et al., 2020a). VNIR spectral analysis by orbiter

99 suggest abundances of 20–65 % clay (Fe-Mg clays) in Mawrth Vallis, representing the highest
100 values measured on Mars (Poulet et al., 2008). Thermal infrared spectra (TIR), indicate a clay
101 abundance of about 15 % in the southern highlands, while the amounts of clays do not exceed 30%
102 in Nili Fossae, Tyrrhena Terra, and Terra Sirenum (Poulet et al., 2008; Ehlmann et al., 2013). Clays
103 and salts may host significant amount of water. Recent estimates of the water content in Gale crater
104 sedimentary sequence show an interquartile range of 2.3–3.1 wt.% H₂O likely associated to
105 adsorbed water, molecular water of hydrated minerals, salts and amorphous phases (Thomas et al.,
106 2020).

107 Based on the stratigraphic distribution of clay and other minerals association, clay deposits on Mars
108 can be associated to three geological environments (Ehlmann et al., 2011; Ehlmann et al., 2013)
109 (Fig.1):

110 i) *crustal clays*, which include Mg-rich smectite (saponite) and chlorite minerals originated from
111 hydrothermal alteration, metamorphism and burial diagenesis (as demonstrated by laboratory
112 experiment (Gaudin et al., 2018; Bishop et al., 2018; Tangari et al., 2020);

113 ii) *stratigraphic clays*, consisting of Fe/Mg smectite overlain by Al- bearing phyllosilicates (as
114 kaolinite, montmorillonite and beidellite), late Noachian to Hesperian in age, often associated with
115 sulphates.

116 iii) *sedimentary clays*, characterized by Fe/Mg smectite often in association with salts and
117 carbonates, found in fluvial and paleolacustrine basins, such as Jezero and Gale Crater (Rampe et
118 al., 2020a; Ehlmann et al., 2009).

119 Owing to the global surface distribution of hydrous minerals and salts, and their susceptibility to
120 fragmentation and pulverization facilitating their spreading across the planet as part of the Martian
121 dust (Ehlmann and Edwards, 2014), grains of salts and hydrous minerals are likely to be present as
122 impurities in the water ice forming the polar caps, and as enriched components of the top layer of
123 regolith at the base of the polar layered deposits.

124

Clays type

 crustal
 stratigraphic
 sedimentary

MAIN MINERALOGY based on Ehlmann et al., 2011-2013	Fe/Mg smectite - chlorite - Al-clays (kaolinite, montmorillonite)- illite	Fe/Mg smectite - chlorite - Al-clays (kaolinite, montmorillonite, other unspecified) - silica - carbonates	Fe/Mg smectite - sulfate - Al-clays (other unspecified)
MARS sites	Argyre, Terra Sirenum, Nili Fossae	Valles Marineris, Arabia Terra	Jezero, Gale, Holden
EARTH analogues	Ch1, Ch2	Sm2, Sm3, Sm4	Sm1

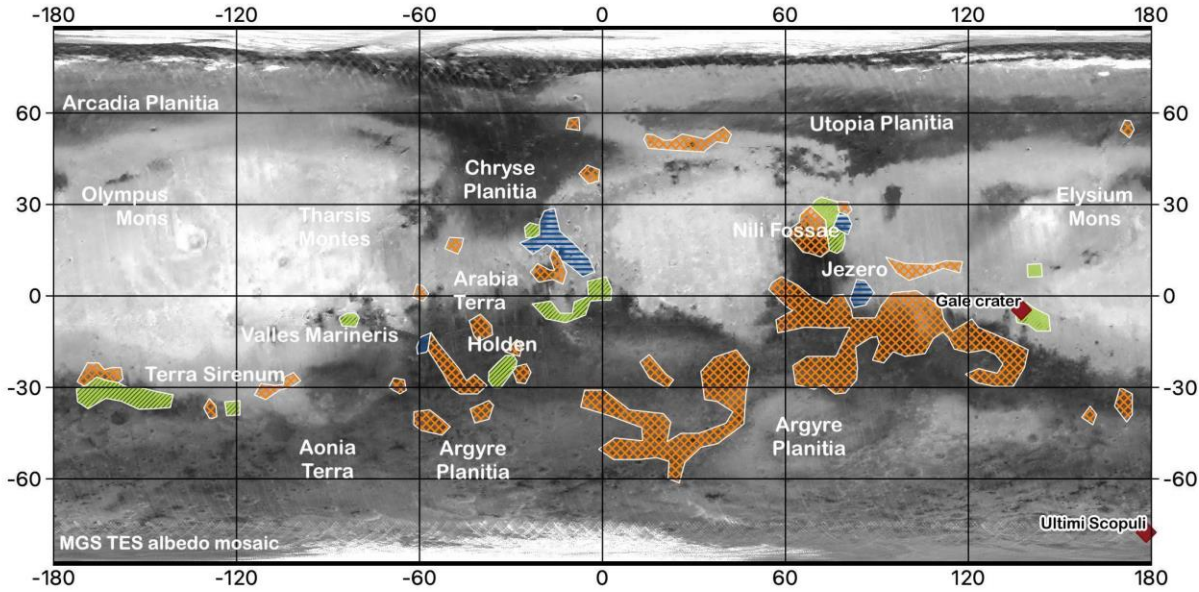


Fig.1. Distribution of clays on Mars. Crustal clays mostly contain Fe-Mg smectite and chlorite as evidence of bedrock alteration. Stratigraphic clays show association of Fe-Mg-Al-rich smectites with carbonates as result of deposition during the wettest period of Mars. Sedimentary clay is often associated with sulfates and chlorides. Potential correlation with used terrestrial analog samples is based on similarities with clay types (ref. to Table S1). Extent and type of clays mapped are from data in Ehlmann et al. (2011) and Ehlmann et al. (2013).

3. An overview on clay and salts dielectric properties

Clay sediments are composite materials: on Earth they are usually made of mineral grains, free water, air, clay aggregates (or clay platelets) and organic matter (Fig.2). Each component of the sediment has a specific dielectric response to an oscillating electric field (e.g., a radar wave) which is described by the complex (relative) dielectric permittivity:

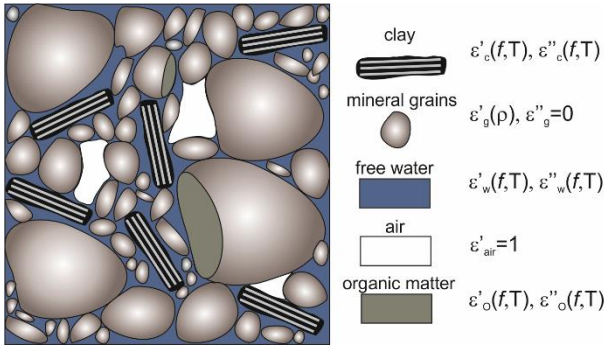
$$\epsilon = \epsilon' + i\epsilon'' \quad (1)$$

The real part of the dielectric permittivity (ϵ') accounts for the polarizability of the material (energy storage) and the imaginary part (ϵ'') for the energy loss due to heat caused by the polarization process (ϵ''_p) and free charge carrier migration (conduction), as follows:

$$\epsilon'' = \epsilon''_p + \frac{\sigma_{DC}}{2\pi f \epsilon_0} \quad (2)$$

145

146 where $\epsilon_0 = 8.85 \cdot 10^{-12} F/m$ is the dielectric permittivity of a vacuum, σ_{dc} is direct-current
 147 conductivity and f is the frequency. The quantities ϵ' and ϵ'' depend on the frequency of the
 148 applied electric field, the temperature of the material (T), water content and salinity (Olhoeft, 1981).
 149 Apart from air (or free space) where $\epsilon' = 1$, the only exception is given by the mineral grains
 150 (including dry clay grains) for which ϵ' only depends on density ρ and ϵ'' is usually negligible
 151 (Olhoeft, 1981; Liu and Mitchell, 2009).



152

153 **Fig. 2.** Sketch of terrestrial unsaturated clay sediment dielectric properties. The overall complex dielectric permittivity
 154 of a sediment is controlled by the volume fraction of the components and their specific dielectric response. Clay
 155 particles are described here by a single value of the real and imaginary parts; however, such values are a combination
 156 of various dielectric responses due to different forms of water inside the clay aggregates. Organic matter, typically
 157 present in surface sediments on Earth, is absent or rare on Mars.

158

159 At a given temperature and for a relative volumetric fraction of each component, the clay sediment
 160 dielectric spectra ($\epsilon'(f)$ and $\epsilon''(f)$) are a complex combination of the different dielectric
 161 responses (Olhoeft, 1977; Lorek and Wagner, 2013). At terrestrial temperatures, the overall (bulk)
 162 complex permittivity is generally dominated by free (salty) water (Fig. 2) as its real and imaginary
 163 parts can be one-three orders of magnitude larger than those of the other components [e.g., Chelidze
 164 et al. (1999), Ishida (2002)]. The dielectric effect of free water is removed if the clay sediment is
 165 oven-dried or desiccated [e.g., Kuligiewicz and Derkowski (2017)]. However, such procedure does
 166 not eliminate bound water, which may still have a high complex permittivity depending on
 167 temperature and frequency (Liu and Mitchell, 2009) and thus could become dielectrically dominant,
 168 especially for clays, such as smectite and vermiculite, that accommodate a large amount of
 169 interlayer water (Lorek and Wagner, 2013; Johnston, 2010). On the other hand, if a wet clay
 170 sediment is cooled below 273 K, free water confined in the pore space of the sediment and in the
 171 clay aggregates starts to freeze, and its contribution to the overall complex permittivity becomes

172 progressively comparable to that of the mineral grains at MARSIS frequencies. Depending on
 173 frequency, the dielectric behavior of bound water could become predominant, controlling the
 174 overall complex dielectric permittivity of the material [e.g., Olhoeft (1977)].

175 As hydrated salts are often associated with clay minerals in the sediments, we first discuss their
 176 contribution to the overall dielectric behavior of clay-rich sediments. Dielectric properties of
 177 hydrated salts have been studied for almost a century [e.g., Burton and Turnbull (1937), Cheng
 178 (1940), Kamiyoshi and Miyamoto (1950), Young and Frederikse (1973)]. It is well known that low
 179 loss characterizes pure salt at frequencies between 1 MHz and 1 GHz, which results in large radar
 180 signal penetration (Stewart and Unterberger, 1976). Dielectric measurements on different types of
 181 hydrated salts in the MHz range at low and high temperatures (ref. to Table 1) indicate that the real
 182 part of permittivity is mainly constant with temperature, and ranges between 4 and 8 (Parkhomenko,
 183 1967), depending on the hydrated state of the crystal (Pettinelli et al., 2016). The imaginary part is
 184 usually very low [e.g., Stewart and Unterberger, Parkhomenko (1967)]: the hydrated magnesian
 185 sulfate meridianiite for example, has an almost constant value of the real part of permittivity in the
 186 temperature interval 200-300 K, and a negligible imaginary part (Pettinelli et al., 2016). The real
 187 part of jarosite is very low, and it is frequency and temperature independent within the range of
 188 temperature 180-296 K and at frequencies between 1 MHz and 1 GHz (Stillman and Olhoeft, 2008).
 189 Additionally, the loss term is below the measurement limit of the instrument, which indicates its
 190 direct-current conductivity is less than 6.67×10^{-5} S/m.

191
 192 **Table 1 Real and imaginary parts of permittivity of some hydrous minerals of interest for Mars.**

Hydrated salts						
	ϵ'	ϵ''	Frequency	Temperature	Reference	Sample
Meridianiite	4.7	~0	1MHz	200K	Pettinelli et al. (2016)	Solid
Jarosite	3.07	~0	1MHz	180-296K	Stillman and Olhoeft, 2008	Granular
Gypsum	6.4	0.01	1 MHz	298K	Olhoeft (1979)	Solid
Anhydrite	6.9	0.06	1 MHz	298K	Olhoeft (1979)	Solid
Dry clay						
Chlorite	7.4	1.5	1 MHz	298K	Olhoeft (1979)	Solid
Kaolinite	4.6	~0	30MHz	298K	Saarenketo (1998)	Solid
Nontronite	3.7	0.08	10MHz	220K	Cunje et al. (2018)	Granular
Ca-montmorillonite (STx-1b)	3.6	0.08	10MHz	220K	Cunje et al. (2018)	Granular
Ca-bentonite	3.5	0.07	1MHz	298K	Saltas et al. (2008)	Granular

201 The dielectric response of clay minerals is particularly complex [e.g., Liu and Mitchell (2009),
 202 Sposito and Prost (1982), Cadène et al. (2006)] due to their retention properties. As smectite is the
 203 most common type of clay mineral detected on Mars, we focus here mainly on the properties of this
 204 group, though all clays share a common dielectric behavior. Smectites have an expanding lattice,
 205 with their layers easily separated by water, and are characterized by a large cation exchange

206 capacity. The number of water molecules that can be accommodated between layers depends on
207 the interlayer cation species and the relative humidity (Johnston, 2010). In general, clay aggregates
208 contain three forms of water: interlayer water, electrostatic double layer water, and free porewater
209 (Wersin et al., 2004). The interlayer water is bound to the exchangeable cations (counterions) and/or
210 to the negatively charged clay particle surfaces, whereas the electrostatic double layer forms a
211 transition zone between the mineral grain surface and the free water confined in the interparticle or
212 interaggregate space. These forms of water have different dielectric response (i.e., different ϵ' and
213 ϵ'') depending on the frequency of the applied electric field and the temperature of the material,
214 which combine in a complicated manner. The dielectric properties of smectites have been
215 extensively studied by several authors at different temperature, frequencies, and water content
216 conditions [e.g., Liu and Mitchell (2009), Sposito and Prost (1982), Cadène et al. (2006), Kaviratna
217 et al. (1996), Kaden et al. (2013)]. In the MHz range, the real part of permittivity of solid clay grains
218 varies between 4 and 8, and remains nearly constant with temperature [e.g., Olhoeft (1979),
219 Saarenketo (1998)] (see Table 1). At low temperature (220 K) dry smectites (montmorillonite and
220 nontronite) exhibit very low values of complex permittivity that do not appreciably change with
221 frequency (Cunje et al., 2018; Kułacz et al., 2021). However, at 298 K and 1 MHz, wet smectite
222 sediments have fairly different dielectric behavior, with real and imaginary parts of permittivity
223 reaching values of the order of 10^2 and 10^3 , respectively (Kaden et al., 2013; Kułacz and
224 Orzechowski, 2019). Conversely, extensive literature data indicate that at low temperature (well
225 below 273 K) the complex dielectric permittivity of wet clay sediments (montmorillonite, bentonite
226 or nontronite enriched) drops significantly, sometimes reaching values close to those of dry clays
227 [e.g., Lorek and Wagner (2013), Cunje et al. (2018), Kułacz and Orzechowski (2019), Moore and
228 Maeno (1993), Bittelli et al. (2004), Stillman et al. (2010)].

230 **4. Radar reflection and apparent permittivity**

231 MARSIS retrieved permittivity values are estimated from the amplitude of the reflected signal. The
232 reflection coefficient Γ_{12} of a normally impinging plane wave at an interface between two adjacent
233 materials depends on the complex dielectric permittivity of such materials (i.e., their dielectric
234 contrast) as follows:

$$\Gamma_{12} = \frac{\sqrt{\varepsilon'_1 + i\varepsilon''_1 + i\frac{\sigma_{1DC}}{2\pi f\varepsilon_0}} - \sqrt{\varepsilon'_2 + i\varepsilon''_2 + i\frac{\sigma_{2DC}}{2\pi f\varepsilon_0}}}{\sqrt{\varepsilon'_1 + i\varepsilon''_1 + i\frac{\sigma_{1DC}}{2\pi f\varepsilon_0}} + \sqrt{\varepsilon'_2 + i\varepsilon''_2 + i\frac{\sigma_{2DC}}{2\pi f\varepsilon_0}}} \quad (3)$$

237

238 Equation (3) shows that Γ_{12} is, in general, a complex quantity, which would require information on
 239 the modulus and phase of the reflected signal to be solved. Conversely, MARSIS data lack the
 240 information on the signal polarity and only allow to estimate $|\Gamma_{12}|$, which is a real quantity.
 241 Therefore, MARSIS does not allow to separately compute real and imaginary parts of the complex
 242 permittivity. Nevertheless, if some assumption on the permittivity of the first layer can be made,
 243 for example that the loss term is negligible ($\varepsilon_1 = \varepsilon'_1$), it is still possible to estimate the dielectric
 244 properties of the second layer introducing the concept of the apparent permittivity ε_a :

245

$$|\Gamma_{12}| = \frac{\sqrt{\varepsilon_a} - \sqrt{\varepsilon_1}}{\sqrt{\varepsilon_a} + \sqrt{\varepsilon_1}} \quad (4)$$

247

248 under the assumption that the permittivity of the second layer is larger than that of the first layer.
 249 Note that Eqn.4 can be slightly modified if the permittivity of the second layer is lower. The quantity
 250 ε_a is analytically obtained as (see Appendix A):

251

$$\varepsilon_a = \varepsilon_1 \left[\frac{1 + |\Gamma_{12}|}{1 - |\Gamma_{12}|} \right]^2 = \varepsilon_1 \frac{\varepsilon_1 + |\varepsilon_2| + \sqrt{\varepsilon_1^2 + |\varepsilon_2|^2 - 2\varepsilon_1\varepsilon'_2}}{\varepsilon_1 + |\varepsilon_2| - \sqrt{\varepsilon_1^2 + |\varepsilon_2|^2 - 2\varepsilon_1\varepsilon'_2}} \quad (5)$$

253

254 It is important to point out that the apparent permittivity is a real quantity that accounts for both
 255 polarization and conductive processes and fully describes the dielectric properties of a material.
 256 Such quantity should not be confused with the real part of permittivity ε'_2 , as it accounts for both
 257 real and imaginary parts of the basal permittivity ε_2 and represents the value that MARSIS would
 258 detect if such material lay below the SPLD. We use equation (5) to compute the apparent
 259 permittivity using real and imaginary parts of published data and laboratory measurements on clay
 260 sediments and salt solutions, assuming for the SPLD a permittivity value $\varepsilon'_1 = 3.5$. Values
 261 computed with Equation (5) were compared to those retrieved from MARSIS data inversion in the
 262 bright reflection area at Ultimi Scopuli (Orosei et al., 2018; Lauro et al., 2021). Specifically, we

will use the median value ($\varepsilon_a = 33$) as the threshold against which to compare and discuss the results in this work. Such median refers to the statistical distribution of the apparent permittivities retrieved by MARSIS at 4 MHz at the base of the SPLD at Ultimi Scopuli (Orosei et al., 2018). Such distribution indicates that there is a probability of 75% to obtain an apparent permittivity value $\varepsilon_a \geq 16$.

5. Analysis of previous studies of dielectric properties of clays at Martian temperatures

We selected published data that allow the estimation of the apparent permittivity at 1 MHz (the closest to MARSIS frequencies common to all available data) for a set of smectites samples having different clay percentage, water content and salt solution concentration (Table 2).

Table 2. Properties and measurement conditions of clay samples used to compute the apparent permittivity at 1MHz from reference data.

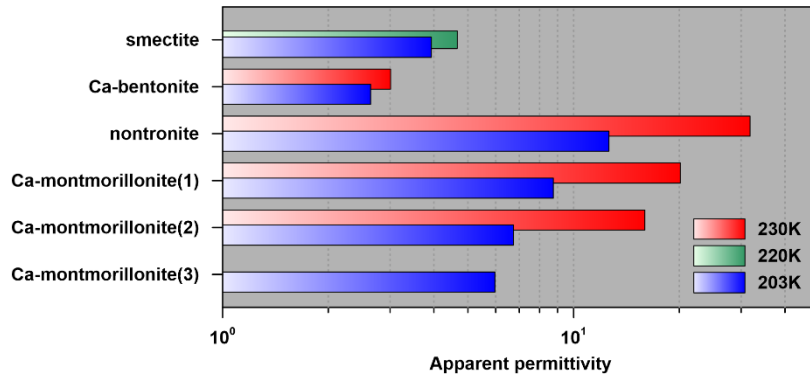
Clay type	Clay content	Water content	Salt solution	Temperature range	Frequency range	Reference
Smectite (Ca-Montmorillonite)	9.67 vol % of STx-1*	0.22-1.34 wt%	1 M CaCl ₂	183K - 298K	1 mHz - 1 MHz	Stillman and Grimm (2011a)
Ca-Bentonite	65-70% wt%	9.27 wt%	-	203K – 293K	10Hz - 1.1 MHz	Lorek and Wagner (2013)
Natural nontronite	(~95 wt%)	21wt%	-	173K – 373K	25 Hz–1 MHz	Kuławcz and Orzechowski (2019)
Ca-Montmorillonite(1)	(20 v% SAz**)	80 v%	0.1 M CaCl ₂	180-298 K	1 mHz - 1 MHz	Stillman et al. (2010)
Ca-Montmorillonite(2)	(20 v% SAz**)	80 v%	0.001 M CaCl ₂	180-298 K	1 mHz - 1 MHz	Stillman et al. (2010)
Ca-Montmorillonite(3)	(46 v% SAz**)	10 v%/44% air	deionized water	180-298 K	1 mHz - 1 MHz	Stillman et al. (2010)

*(>95% montmorillonite)

**(>95% montmorillonite)

Among those, we selected two temperatures: 203K, the lowest value common to all measurements reported in Table 2 and 230K a temperature slightly higher than the mean surface temperature on Mars (~220K in Stillman and Grimm (2011a)). The apparent permittivity of the dataset computed at 1 MHz highlights the large variability (from 2.6 to 31.8) of the clay dielectric response (Fig. 3). Smectite and Ca-bentonite samples exhibit the lowest values (2.6-4.7) (Table 2) probably because of low water content, that do not appreciably change with temperature. The apparent permittivity of the Ca-montmorillonite and nontronite samples at 203 K does not exceed 13; however, at 230 K the apparent permittivity of the Ca-montmorillonite increases up to 20.1 for sample 1 and 16.0 for sample 2, respectively. Such increase is probably due to the liquid brines in the samples, as they were prepared by mixing the clay with a large amount of CaCl₂ solutions (Table 2), which has an eutectic temperature < 230 K (Grimm et al., 2008). The highest value is reached by the almost pure sample (95%) of natural nontronite with 21% of water content (Kuławcz and Orzechowski, 2019). These data suggest that for a temperature at the base of the SPLD > 230 K, some of the analyzed

292 clay samples could potentially produce relatively strong reflections. However, according to both
 293 theoretical and experimental evidence, the apparent permittivity of clay sediments should decrease
 294 at higher frequencies [e.g., Lorek and Wagner (2014), Kułacz and Orzechowski (2019), Stillman
 295 and Grimm (2011b), Kao (2004)]. Therefore, values at 1 MHz should be considered an
 296 overestimation relative to those measured at 4 MHz and must therefore be corrected before being
 297 compared with MARSIS data.

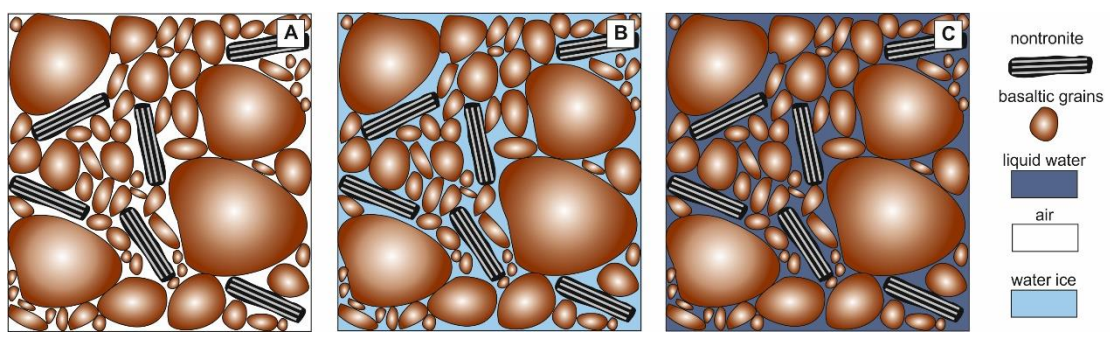


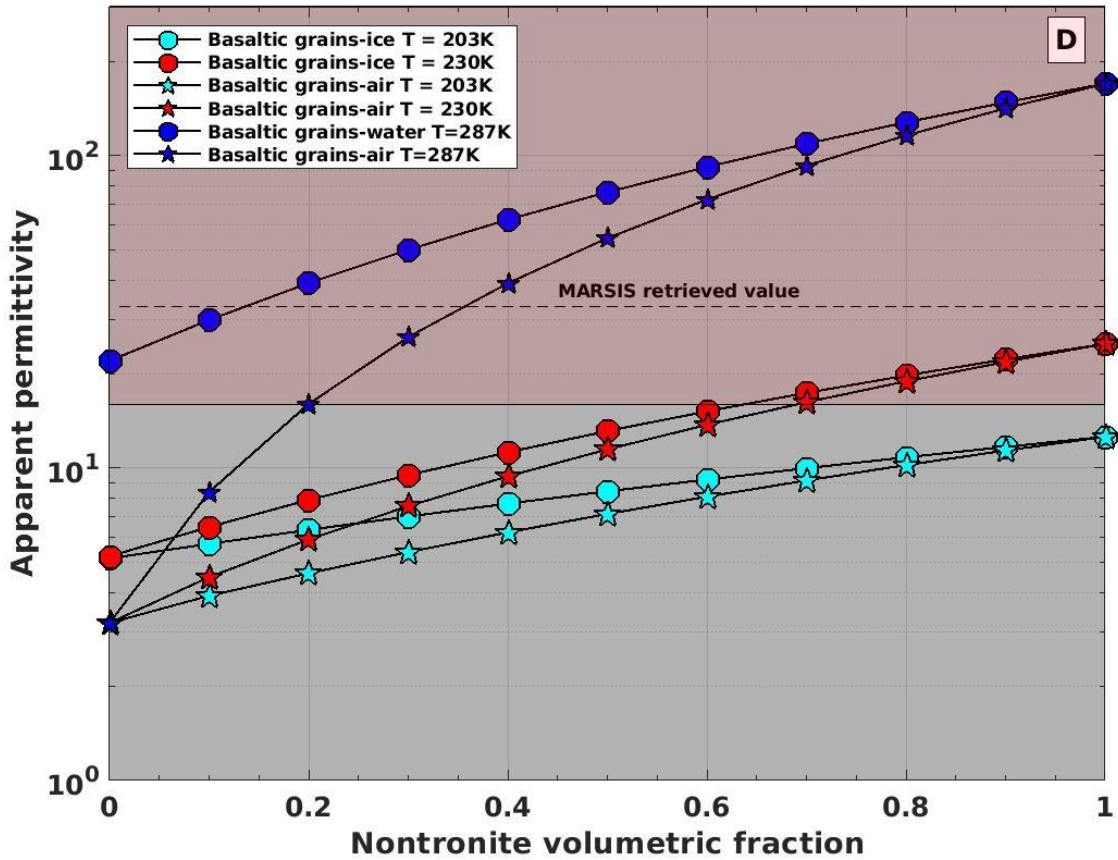
299 **Fig. 3** Apparent permittivity at 1 MHz from literature data. Values of the apparent permittivity computed at 203 K and
 300 230 K (220 K is from Stillman and Grimm (2011a), ref. to Table 2) from real and imaginary parts measured at 1 MHz
 301 on various smectite samples. The samples have different water content, clay content and salt solutions (Table 2).

302
 303 Because the nontronite sample exhibits the highest apparent permittivity and is a common mineral
 304 in the Martian clay sediments, we used Kułacz and Orzechowski's (2019) experimental dataset to
 305 compute its apparent permittivity at 4 MHz, by shifting low temperature data to higher frequencies
 306 (according to the method proposed by Stillman and Grimm (2011a)). After correction, we found that
 307 the apparent permittivity at 203 K did not appreciably change from that at 1 MHz (~13), whereas
 308 at 230 K the value at 4 MHz decreases to 25.1. Moreover, as the nontronite sample is almost pure
 309 and the clay content detected in Martian terrains is highly variable (ranging between 3 and 65 wt%)
 310 we used the Complex Refractive Index Model (CRIM) (Sihvola, 1999) to evaluate the effect of the
 311 nontronite content (expressed in volume fraction) on the overall apparent permittivity of a clay
 312 sediment (Fig. 4). We assumed the composition of the sediments to be: i) basaltic grains, air and
 313 nontronite (desiccated Martian model) (Fig. 4A); ii) basaltic grains, water ice and nontronite (water
 314 ice saturated Martian model) (Fig. 4B); and iii) basaltic grains, liquid water and nontronite
 315 (terrestrial analog) (Fig. 4C). Mixing models were computed at 203 K, 230 K and 287 K for a
 316 volume fraction of nontronite ranging from 0 to 1. Permittivity values for the basalt grains and
 317 water ice are those published by Mattei et al. (2014), liquid water values are from Kaatz (1989),
 318 and those for natural nontronite (21 wt% H₂O) are by Kułacz and Orzechowski (2019). As expected,

319 the apparent permittivity values computed at 230 K are higher than those at 203 K and the values
320 computed for the model with water ice in the pores are slightly larger than those with air-filled
321 pores (Fig. 4D). The nontronite content produces a clear increase in the overall apparent
322 permittivity: for example, 50% of nontronite content increases the apparent permittivity from 5.2
323 (0%) to 13.1 in the simulation with ice. Even so, both plots at 203 K and 230 K are below MARSIS
324 threshold value ($\epsilon_a = 33$), converging toward the values of (almost) pure nontronite at 4 MHz (25.1
325 at 230 K and 12.6 at 203 K). Conversely, in the terrestrial water-saturated clay sediment simulation
326 (287 K) MARSIS retrieved value is reached with 14% of nontronite content, whereas for dry sediment,
327 we need at least 35% of nontronite volume fraction. The pink shaded area in Fig.4D
328 delimits the region where the apparent permittivity values are above 16 (75% of the population of
329 MARSIS retrieved basal permittivity). It is interesting to note that only samples at 230K containing
330 at least 70% of nontronite fall inside this area.

331





332
 333 **Fig. 4** Effect of nontronite content on the apparent permittivity from CRIM simulations at 4 MHz. A) desiccated
 334 Martian model; B) water ice saturated Martian model; C) terrestrial analogue. D) Different colors and shapes indicate
 335 different temperatures and mixtures: dots represent ice or water saturated mixtures; stars are dry samples (with air-
 336 filled pores). The ratio between the volume fraction of the basaltic grains and the material in the pore is held constant
 337 (1.5), with the nontronite volume fraction progressively increasing. The black dashed line indicates the MARSIS
 338 threshold value $\epsilon_a = 33$; pink area highlights the apparent permittivity interval for which the probability that the
 339 permittivity assumes values $\epsilon_a \geq 16$ is 75%.

341 6. Laboratory dielectric measurements

343 6.1 Martian clay sediments analogs

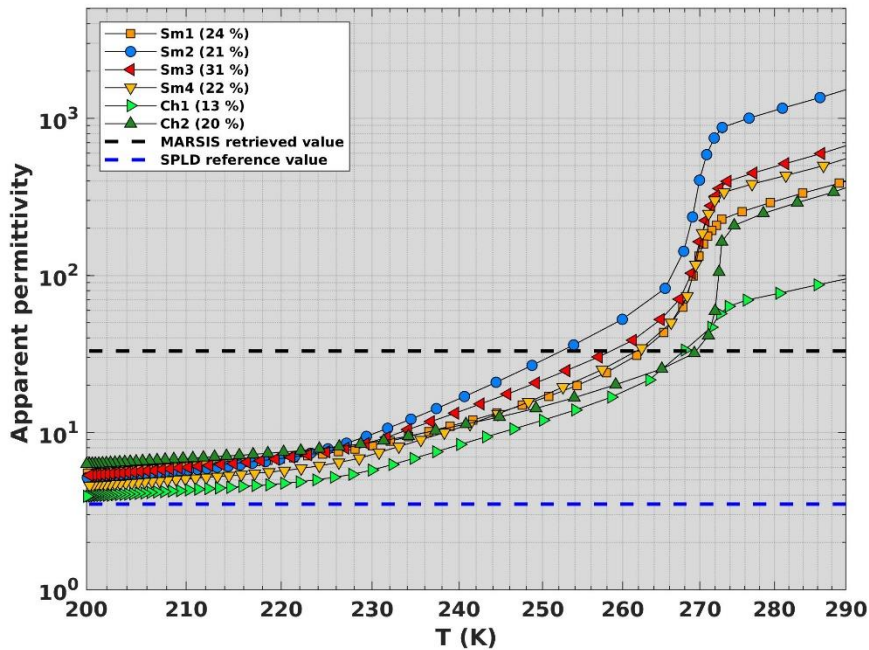
344 We complemented literature data with new experimental results. We performed a set of laboratory
 345 measurements, selecting six clay samples collected in Italy in different geological settings: recent
 346 Holocene (< 12,000 years) fluvial deposits, Pliocene-Early Pleistocene (< 5 million years) marine
 347 mudstone, and metamorphic deposits dated from Jurassic to Oligocene (< 200 million years). The
 348 samples were mostly selected based on clay mineralogy (Table S1) which makes them good analogs
 349 for Martian clays (Fig. 1). The clay mineralogy and percentage of clay in the sediments were

350 determined by X-ray diffraction (XRD) (ref. to Fig.S1 and Appendix B) enabling us to directly
351 compare our data with the analysis performed by the XRD instrument (CHEMIN) in Gale crater
352 (Rampe et al. 2020a). We also considered the overall distribution of clays on Mars based on spectral
353 investigations from orbiter to have a more global context and variability of Martian clays (Fig.1).
354 Identified clay minerals in our samples are smectite, illite, kaolinite, and chlorite (only present in
355 two samples) with variable quantities as also observed in Gale crater (ref. to Table S1; Fig. S1).
356 The samples were sieved at 75 μ m and oven-dried at 105°C until their weight remained constant,
357 and then rehydrated with distilled water until they returned to initial water content (13-31 wt%).
358 For one clay sample we also collected a series of measurements for different water contents to
359 evaluate the dielectric properties of clays at dry or low water content. Measurements were
360 performed while the samples slowly warmed up from an initial temperature of 200 K, to ensure
361 thermal equilibrium inside the sample during each frequency sweep. Real and imaginary parts as a
362 function of frequency and temperature were measured using a coaxial transmission line and a
363 Vector Network Analyzer (Mattei et al., 2013), in the frequency range 1 MHz-1 GHz and over the
364 temperature interval 200 K – 298 K (Appendix C). Data are reported as apparent permittivity vs.
365 temperature at 4 MHz (Fig. 5) to allow a direct comparison with the basal apparent permittivity
366 retrieved by MARSIS (Orosei et al., 2018).

367 All clay samples show a similar trend: at 200 K the apparent permittivity ranges between 4.0 (Ch1)
368 and 6.4 (Sm2) and slightly increases (curves almost parallel) up to 224 K, at which point the values
369 start to diverge. At about 230 K, values of apparent permittivity range between 6 (Ch1) and 10
370 (Sm2). At 252 K, the sample Sm2 reaches MARSIS threshold value. The same threshold is reached
371 by sample Sm3 at 258 K, samples Sm1 and Sm4 at 262 K and samples Ch1 and Ch2 at about 268
372 K. Above 265 K, ice melting produces a steep increase in the apparent permittivity, whereas above
373 273 K the trend changes to a gentler slope as ice is totally molten. At a temperature of 290 K the
374 apparent permittivity reaches values ranging between 10^2 - 10^3 , with Ch1 (13% water content,
375 chlorite sample) being the lowest and Sm2 (21% water content, smectite sample) the highest.
376 Moreover, the measurements collected on sample Sm4 at different water contents (Fig. S2) show
377 that for low values of saturation (3.5% and 5.6% water content) the apparent permittivity at 273 K
378 is around 10, reaching the MARSIS threshold value at 276 K with 14% of water content. No clear
379 correlation between apparent permittivity and water content, clay content or clay mineralogy is
380 recognizable in the data set (Fig.1 and Table S1), confirming the complexity of clay sediments
381 dielectric behavior reported in the literature [e.g., Liu and Mitchell (2009), Lorek and Wagner
382 (2013), Ishida (2002), Cadène et al. (2006)]. Moreover, data plotted as a function of frequency (Fig.
383 S3) clearly show that both real and imaginary parts decrease when frequency increases, confirming

384 that in clay sediments caution should be taken when using values at 1 MHz to interpret radar data
385 collected at 4 MHz.

386



387

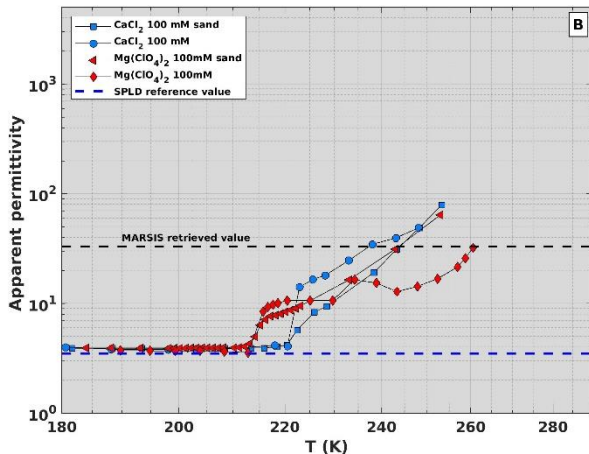
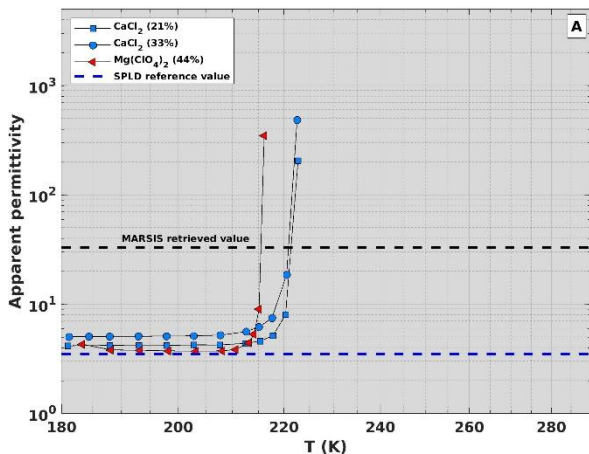
388 **Fig.5** Apparent permittivity at 4 MHz from experimental data. Apparent permittivity computed from real and imaginary
389 parts measured at 4 MHz as a function of temperature on four smectite-rich (Sm) and two chlorite-rich (Ch) sediments
390 having different water content (% in the legend). Black dashed line indicates the threshold $\epsilon_a = 33$ retrieved by
391 MARSIS, and blue dashed line the SPLD ice permittivity value ($\epsilon_1' = 3.5$) used to compute the apparent permittivity.
392 For clarity uncertainties are not shown in the diagram: they represent few percent of the measured values.

393

394 **6.2 Mg(ClO₄)₂ and CaCl₂ brines at Martian subglacial conditions**

395 Previous works (Orosei et al., 2018; Lauro et al., 2021) suggested brines as the most plausible cause
396 of MARSIS strong reflections as salty solutions can have very high complex permittivity (Addison,
397 1975). We quantify here the dielectric response of Mg(ClO₄)₂ and CaCl₂ brines at Martian
398 subglacial conditions by computing the apparent permittivity as a function of temperature at 4 MHz
399 from published (Stillman et al., 2010; Stillman and Grimm, 2011a; Grimm et al., 2008; Stillman
400 and Grimm, 2011b) and unpublished (measurement methodology is the same as Stillman et al.
401 (2010)) data. We considered pure solutions for high salt concentrations (Mg(ClO₄)₂ 44% wt, CaCl₂
402 33% wt, and CaCl₂ 21% wt) and both pure solutions and saturated sand for low salt concentrations
403 (100 mM for both Mg(ClO₄)₂ and CaCl₂). Measurements were taken between 180 K and 270 K,
404 noting however that, once the ice starts melting, the imaginary part dominates the measured signal,
405 and the real part cannot be measured accurately. Well below the eutectic temperature (216 K for

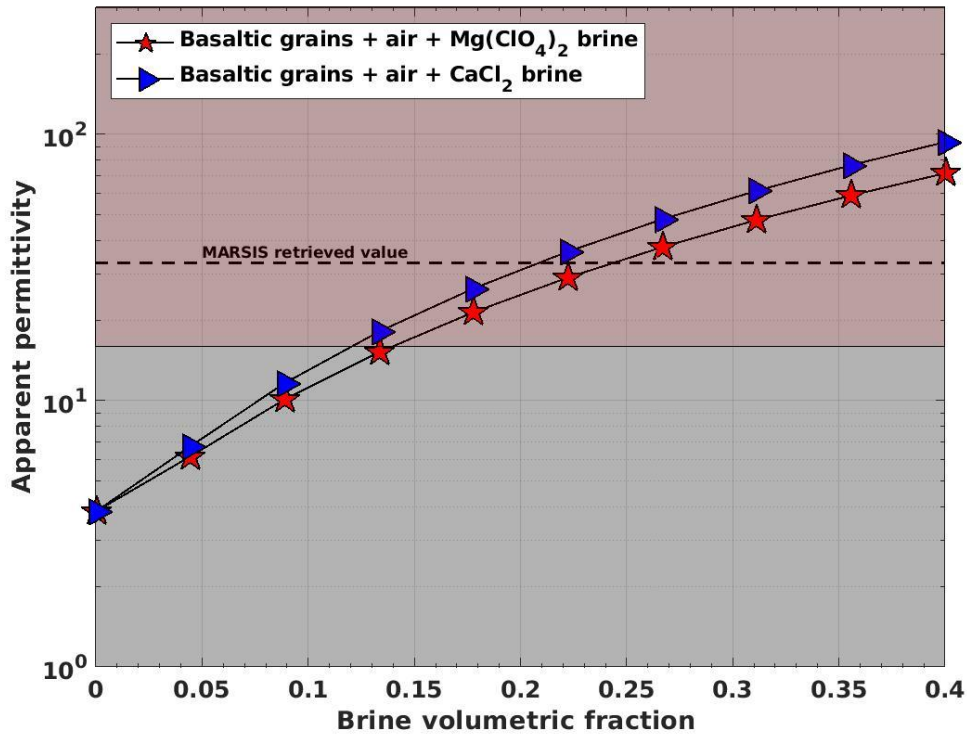
406 $\text{Mg}(\text{ClO}_4)_2$, and 222 K for CaCl_2) all saline solutions exhibit apparent permittivity values around
 407 4, with the exception of the CaCl_2 at 33% (slightly hypereutectic) which is slightly higher (~ 5),
 408 probably due to the contribution of the salt grain inclusions in the ice [e.g., Pettinelli et al. (2016)]
 409 (Fig. 6A). These values indicate that, once a saline ice is completely frozen, the values of both real
 410 and imaginary parts are very low, and thus do not produce a strong dielectric contrast with the
 411 SPLD ice, irrespective of the concentration of salt. When the ice approaches the eutectic
 412 temperature, it starts to melt, generating an abrupt increase in both real and imaginary parts and in
 413 the apparent permittivity. At the eutectic temperature, for salt content around the eutectic
 414 concentration, the ice is largely or totally molten, and the apparent permittivity is higher than 10^2 ,
 415 well above the MARSIS threshold value (Fig. 6A). The volume fractions of the brines in each
 416 sample can be estimated from the eutectic temperature which is very close to the temperature where
 417 the curves intersect the threshold; we found 74% of brine content for CaCl_2 at 33% wt, 100% for
 418 $\text{Mg}(\text{ClO}_4)_2$ at 44% wt (eutectic concentration), and 44% for CaCl_2 at 21% wt. The dielectric response
 419 of the low concentration solutions is clearly different (Fig. 6B). Although an abrupt increase in
 420 apparent permittivity occurs around the eutectic temperature, its magnitude is much smaller:
 421 MARSIS threshold is reached by the pure CaCl_2 solution at ~ 240 K (Fig. 6B), and at higher
 422 temperatures by the other samples. The brine volume fractions at such temperatures are low (1.4 -
 423 6.0%), but the high value of the apparent permittivity is justified as briny liquid vein networks form,
 424 which drastically increase the conductivity once the temperature of the sample is above that of the
 425 eutectic. Because salt is nearly insoluble in ice (Gross et al., 1977; Stillman et al., 2013), the salts
 426 and their resulting brines tend to concentrate along grain boundaries (Grimm et al., 2008).
 427



429 **Fig.6** Apparent permittivity of brines at 4 MHz as a function of temperature. A) Apparent permittivity of brine/ice
430 samples starting from 21% and 33% wt CaCl₂ and 44% wt Mg(ClO₄)₂ solutions. B) Apparent permittivity of CaCl₂ and
431 Mg(ClO₄)₂ salty ice/sand mixtures with 100 mM salt solutions. Two brine/ice samples with CaCl₂ and Mg(ClO₄)₂ and
432 two CaCl₂ and Mg(ClO₄)₂ ice/sand mixtures with 46% (CaCl₂) and 57.1% (Mg(ClO₄)₂) volumetric fraction of admixed
433 sand were measured. Black dashed line indicates the threshold $\epsilon_a = 33$ retrieved by MARSIS, and blue dashed line the
434 SPLD ice permittivity value ($\epsilon_1' = 3.5$) used to compute the apparent permittivity.

435

436 Finally, we used measured data and three-phases CRIM to evaluate the effect of eutectic or slightly
437 hypereutectic brine volume fractions on the overall apparent permittivity of a sandy soil (regolith)
438 (Fig. 7). For the complex permittivity of basaltic grains we used values from Mattei et al. (2014)
439 and for the brines those retrieved from Mg(ClO₄)₂ (44%wt) and CaCl₂ (33%wt) samples at the
440 eutectic temperature (Fig. 6A). The simulations compute the apparent permittivity of a soil with
441 pores progressively saturated with brines. Even though the CaCl₂ (33% wt) is not an exact eutectic
442 concentration, it is however close enough to produce reliable values. The results of the simulations
443 do not appreciably differ, with the MARSIS threshold value reached by sand/CaCl₂ brine mixtures
444 at about 21% of brines volume fraction, and by sand/Mg(ClO₄)₂ brine mixture at about 25% (Fig.
445 7). Note that for brines volume fraction higher than 15% the apparent permittivity is above 16 (pink
446 area in Fig.7). For a fully saturated soil (40% porosity) the apparent permittivity of the sand/CaCl₂
447 brine mixtures is ~94 and for the sand/Mg(ClO₄)₂ brine mixture it is close to 71.



448 **Fig.7** Effect of brines contents on the apparent permittivity of a soil from CRIM simulations at 4MHz. Apparent
 449 permittivity computed for a sandy soil with 40% porosity, from dry to brines saturated conditions. Blue triangles
 450 (33%wt CaCl₂) refer to the apparent permittivity measured at ~222K and red stars (44%wt Mg(ClO₄)₂) to the apparent
 451 permittivity measured at ~216K. Black dashed line indicates the threshold $\epsilon_a = 33$ retrieved by MARSIS; pink area
 452 highlights the apparent permittivity interval for which the probability that the permittivity assumes values $\epsilon_a \geq 16$ is
 453 75%.

454 7. Discussion and Conclusion

455 Data collected by MARSIS and SHARAD in the areas where hydrated minerals have been found
 456 and/or where they are particularly abundant (Fig.1), do not show any indication of bright reflections
 457 coming from the surface. Given the cold temperatures and low water content estimated on Mars
 458 (2.3–3.1 wt.% H₂O) (Thomas et al., 2020), clay minerals have been considered a concern for radar
 459 attenuation but not a strong surface reflector, capable of preventing radar signals penetrating
 460 through the surface (Stillman and Grimm, 2011a; Cunje et al., 2018). These observations are in
 461 good agreement with literature data (Ca-bentonite sample in Fig. 3) and with our experimental
 462 results (Fig. S2), which show that hydrated salts and dry or low water content clay, do not generate
 463 strong radar reflections on the Martian surface or at the base of the SPLD (Table 1). Consequently,
 464 even if present in large amount in the basal sediments, hydrated salts and dry clay would exhibit
 465 apparent permittivity similar or of even lower than the SPLD ice (see Fig.S2).

466 Temperature has a dominating effect on the dielectric properties of clay and clay sediments (Lorek
467 and Wagner, 2013; Moore and Maeno, 1993; Bittelli et al., 2004). High values (25.1), such as those
468 shown at 230 K by almost pure nontronite (21% water content), are reduced by half (12.6) when
469 the temperature drops to 203 K. At this temperature, a clay sediment containing 60% of nontronite
470 does not exceed an apparent permittivity value of 9 (Fig. 4D). The drastic effect of temperature on
471 the dielectric behavior of clays is confirmed by our set of measurements conducted on clay
472 sediments at different water content, clay content, and different mineralogy: the MARSIS threshold
473 value is only obtained at high temperature ($\geq 250\text{K}$). At 203 K the apparent permittivity of the clay
474 sediments does not exceed 7, a value not dissimilar from the apparent permittivity values reported
475 for the hydrated salts or dry clay (Table 1). Comparing published data, simulations, and laboratory
476 measurements, we found that at 4 MHz and 230 K, the apparent permittivity of clay sediments,
477 even with a very high percentage of clay (70% volume fraction of nontronite) barely exceeds 16,
478 while at 203 K it does not go beyond 10. It follows that very low temperatures, such as those
479 commonly inferred at the base of the SPLD ($\leq 200\text{K}$), are totally inconsistent with the hypothesis
480 that clay sediments can generate a dielectric contrast with the SPLD large enough to obtain bright
481 basal echoes.

482 Our dielectric measurements on $\text{Mg}(\text{ClO}_4)_2$ and CaCl_2 brines at Martian subglacial conditions rule
483 out also salty ice as the cause for MARSIS bright reflections. Totally frozen brines having high
484 concentration of salts exhibit very low apparent permittivity, because salt grain inclusions do not
485 appreciably change the dielectric properties of the ice at MARSIS frequencies (Fig. 6A). These
486 results are supported by published data on the dielectric properties of sea ice at very low temperature
487 [e.g., Addison (1975), Fujino (1967)]. The apparent permittivity at low salt concentration (100 mM)
488 does not exceed 10-15 at the eutectic temperature. However, our results (Fig. 6B) suggest that a
489 few 100s mM of salt would probably be enough to reach the MARSIS threshold value (Stillman et
490 al., 2021). Vice versa, given the very large apparent permittivity values measured for both
491 $\text{Mg}(\text{ClO}_4)_2$ and CaCl_2 brines at high salt concentrations (Fig. 6A), a few 10s percent of liquid brine
492 volume fraction in the ice or in the soil would probably be sufficient to enhance the overall apparent
493 permittivity well above the MARSIS retrieved value (Fig.6A and Fig.7). Thus, based on their
494 dielectric behavior alone, $\text{Mg}(\text{ClO}_4)_2$ and CaCl_2 brines appear to be the preferable candidates to
495 explain MARSIS bright basal reflections observed in Ultimi Scopuli (Orosei et al., 2018; Lauro et
496 al., 2021). It has been argued that the eutectic temperatures of brines are too high to explain the
497 presence of liquid water at the base of the SPLD (Sori and Bramson, 2019). Previous studies have
498 found that salts with large freezing point depressions also have large metastable eutectic
499 temperatures that can be 10s of degrees lower than their eutectic temperature (Toner and Catling,

2018; Primm et al., 2020). Our measurements were performed after freezing the salt solutions to much colder temperature (<188 K) than the eutectic temperatures. For example, the 100 mM Mg(ClO₄)₂ sample was held at 193 K for 72 hours and never fully froze, until the temperature was reduced to 188 K. We can expect that other perchlorates like Ca(ClO₄)₂ (eutectic temperature ~198 K) would exhibit a dielectric response similar to the salts investigated in this work, but at lower temperature. Additionally, it has been proven that a mixture of Ca and Mg perchlorate has eutectic temperature well below those of the single salts (Nair and Unnikrishnan, 2020) and the brines can remain in a supercooled state at temperatures as low as 150 K (Toner et al., 2014). Whether supercooled salty waters can persist in subglacial environments over geologic timescales is still an open issue. Future work will need to focus on the specific question of the longevity of brines in hyperarid cold conditions. Metastability aside, however, another poorly constrained parameter is the thermal conductivity of the SPLD deposits, which directly bears on estimated values of basal temperatures: Sori and Bramson (2019) argue that under the current (and most likely) value of heat flux at the south polar region of Mars, the temperature at the base of the SPLD in Ultimi Scopuli is < 180 K. However, their model involves a highly conductive SPLD, which is far from being conclusively demonstrated. In fact, small variations in estimated values of conductivity of the SPLD materials, could dramatically increase basal temperatures to values equal to or even above those of perchlorate brine eutectics.

518
519
520
521

522 **Appendix A**

523 The absolute value of the reflection coefficient Γ_{12} can be rewritten as:

$$524 \quad |\Gamma_{12}| = \left| \frac{\sqrt{\epsilon_2} - \sqrt{\epsilon_1}}{\sqrt{\epsilon_2} + \sqrt{\epsilon_1}} \right| \quad (6)$$

525 The complex permittivity of the second medium can be expressed in terms of its module and
526 phase as:

$$527 \quad \epsilon_2 = \epsilon_2' + i\epsilon_2'' = |\epsilon_2| e^{i\theta} = |\epsilon_2| (\cos \theta + i \sin \theta) \quad (7)$$

528 With

$$\cos \theta = \frac{\varepsilon_2'}{|\varepsilon_2|}$$

$$\sin \theta = \frac{\varepsilon_2''}{|\varepsilon_2|}$$

530 As a consequence, using the bisection rules, the square root of ε_2 is given by:

$$531 \quad \sqrt{\varepsilon_2} = \sqrt{|\varepsilon_2|} e^{i\frac{\theta}{2}} = \sqrt{|\varepsilon_2|} \left(\cos \frac{\theta}{2} + i \sin \frac{\theta}{2} \right) = \sqrt{|\varepsilon_2|} \left(\sqrt{\frac{1+\cos \theta}{2}} + i \sqrt{\frac{1-\cos \theta}{2}} \right)$$

532 Replacing the last equation in Equation 6 we have:

$$533 \quad |\Gamma_{12}| = \frac{\left| \sqrt{|\varepsilon_2|} \sqrt{1+\cos \theta} - \sqrt{2\varepsilon_1} + i \sqrt{|\varepsilon_2|} \sqrt{1-\cos \theta} \right|}{\left| \sqrt{|\varepsilon_2|} \sqrt{1+\cos \theta} + \sqrt{2\varepsilon_1} + i \sqrt{|\varepsilon_2|} \sqrt{1-\cos \theta} \right|} \quad (8)$$

534 The absolute value of Γ_{12} is given by,

$$535 \quad |\Gamma_{12}| = \frac{\sqrt{\left(\sqrt{|\varepsilon_2|} \sqrt{1+\cos \theta} - \sqrt{2\varepsilon_1} \right)^2 + \left(\sqrt{|\varepsilon_2|} \sqrt{1-\cos \theta} \right)^2}}{\sqrt{\left(\sqrt{|\varepsilon_2|} \sqrt{1+\cos \theta} + \sqrt{2\varepsilon_1} \right)^2 + \left(\sqrt{|\varepsilon_2|} \sqrt{1-\cos \theta} \right)^2}} =$$

$$= \frac{\sqrt{|\varepsilon_2| (1+\cos \theta) - 2\sqrt{2\varepsilon_1} |\varepsilon_2| \sqrt{1+\cos \theta} + 2\varepsilon_1 + |\varepsilon_2| (1-\cos \theta)}}{\sqrt{|\varepsilon_2| (1+\cos \theta) + 2\sqrt{2\varepsilon_1} |\varepsilon_2| \sqrt{1+\cos \theta} + 2\varepsilon_1 + |\varepsilon_2| (1-\cos \theta)}} = \quad (9)$$

$$= \frac{\sqrt{|\varepsilon_2| - \sqrt{2\varepsilon_1} |\varepsilon_2| \sqrt{1+\cos \theta} + \varepsilon_1}}{\sqrt{|\varepsilon_2| + \sqrt{2\varepsilon_1} |\varepsilon_2| \sqrt{1+\cos \theta} + \varepsilon_1}} = \frac{\sqrt{|\varepsilon_2|^2 + \varepsilon_1^2 - 2\varepsilon_1 |\varepsilon_2| \cos \theta}}{|\varepsilon_2| + \varepsilon_1 + \sqrt{2\varepsilon_1} |\varepsilon_2| \sqrt{1+\cos \theta}}$$

536 Now, we want to estimate ε_a that is the quantity for which we can write the reflection coefficient

537 like a real quantity, i.e.:

$$538 \quad |\Gamma_{12}| = \frac{\sqrt{\varepsilon_a} - \sqrt{\varepsilon_1}}{\sqrt{\varepsilon_a} + \sqrt{\varepsilon_1}} \quad (10)$$

539 From equation (10) it follows:

$$540 \quad \varepsilon_a = \varepsilon_1 = \left(\frac{1+|\Gamma_{12}|}{1-|\Gamma_{12}|} \right)^2 = \varepsilon_1 \frac{1+|\Gamma_{12}|^2 + 2|\Gamma_{12}|}{1+|\Gamma_{12}|^2 - 2|\Gamma_{12}|} \quad (11)$$

541 From equation (9) we can calculate $|\Gamma_{12}|^2$:

542
$$|\Gamma_{12}|^2 = \frac{\varepsilon_1 + |\varepsilon_2| - \sqrt{2\varepsilon_1|\varepsilon_2}\sqrt{1 + \cos\theta}}{\varepsilon_1 + |\varepsilon_2| + \sqrt{2\varepsilon_1|\varepsilon_2}\sqrt{1 + \cos\theta}} \quad (12)$$

543 It follows that

544
$$1 + |\Gamma_{12}|^2 \pm 2|\Gamma_{12}| = 2 \frac{\varepsilon_1 + |\varepsilon_2| \pm \sqrt{|\varepsilon_2|^2 + \varepsilon_1^2 - 2\varepsilon_1|\varepsilon_2|\cos\theta}}{\varepsilon_1 + |\varepsilon_2| + \sqrt{2\varepsilon_1|\varepsilon_2}\sqrt{1 + \cos\theta}} \quad (13)$$

545 Replacing equation (13) in equation (10), we obtain:

546
$$\begin{aligned} \varepsilon_a &= \varepsilon_1 \frac{\frac{\varepsilon_1 + |\varepsilon_2| + \sqrt{|\varepsilon_2|^2 + \varepsilon_1^2 - 2\varepsilon_1|\varepsilon_2|\cos\theta}}{\varepsilon_1 + |\varepsilon_2| + \sqrt{2\varepsilon_1|\varepsilon_2}\sqrt{1 + \cos\theta}}}{\frac{\varepsilon_1 + |\varepsilon_2| - \sqrt{|\varepsilon_2|^2 + \varepsilon_1^2 - 2\varepsilon_1|\varepsilon_2|\cos\theta}}{\varepsilon_1 + |\varepsilon_2| + \sqrt{2\varepsilon_1|\varepsilon_2}\sqrt{1 + \cos\theta}}} = \\ &= \varepsilon_1 \frac{\varepsilon_1 + |\varepsilon_2| + \sqrt{|\varepsilon_2|^2 + \varepsilon_1^2 - 2\varepsilon_1|\varepsilon_2|\cos\theta}}{\varepsilon_1 + |\varepsilon_2| - \sqrt{|\varepsilon_2|^2 + \varepsilon_1^2 - 2\varepsilon_1|\varepsilon_2|\cos\theta}} = \\ &= \varepsilon_1 \frac{\varepsilon_1 + |\varepsilon_2| + \sqrt{\varepsilon_1^2 + |\varepsilon_2|^2 - 2\varepsilon_1\varepsilon_2'}}{\varepsilon_1 + |\varepsilon_2| - \sqrt{\varepsilon_1^2 + |\varepsilon_2|^2 - 2\varepsilon_1\varepsilon_2'}} \end{aligned}$$

547 That is the expression of the apparent permittivity given in equation (5).

548

549 **Appendix B**

550 **X-ray Diffraction analysis (XRD)**

551 Mineralogical analysis was performed using the Rigaku MiniFlex II X-ray diffractometer with Cu-
 552 Ka radiation, monochromated with graphite and operated at 30 kV and 15 mA. The diffraction
 553 pattern was acquired on bulk powder samples obtained by grinding small pieces of rock with
 554 mechanical agata mortar and pestle. The XRD patterns were collected in the 3–50 2θ range which
 555 is representative of the main mineral species diffraction peaks. The different mineralogical species
 556 were identified by matching the peaks with the reference Crystallography Open Database (COD
 557 2020) using the Match! software (version 3.10.2). Semi-quantitative analysis was performed using
 558 a Reference Intensity Ratio method (RIR-method) included in the Match! software (version 3.10.2).
 559 This analysis is based on I/Ic factor indicating the ratio between the intensity of the highest peak
 560 diffraction of the identified phase in comparison with the highest peak of Corundum standard.

561

Appendix C

Dielectric measurements

The experimental set-up consists of a two-port Vector Network Analyzer (Agilent E5071C) connected through two cables to a coaxial-cage line (cell) filled with the material under test. The measuring cell is a stainless-steel cage housed in a plexiglass box; it consists of a central conductor and an outer structure made by eight equally spaced rods arranged in a cylindrical pattern. Detailed description of the setup can be found elsewhere (Mattei et al., 2013). The experimental setup allows to retrieve the dielectric properties of the material under test (in terms of complex dielectric permittivity and complex magnetic permeability), applying the Nicolson-Ross-Weir algorithm (Nicolson and Ross, 1970; Weir, 1974). The fundamental equations are given by:

$$\sqrt{\frac{\varepsilon}{\mu}} F_g = \frac{1-\Gamma}{1+\Gamma} \quad (14)$$

$$\sqrt{\varepsilon\mu} l = \frac{jc}{2\pi f} \ln(\Psi) \quad (15)$$

where Γ and Ψ are the reflection and transmission coefficients through the coaxial line, ε and μ are the complex relative dielectric permittivity and magnetic permeability, respectively, F_g is a geometrical factor that accounts for the impedance mismatch between the coaxial cables and the coaxial-cage line in air, l is the length of the coaxial-cage line and c is the velocity of the light in a vacuum. Combining Equation (14) and (15), the complex dielectric permittivity can be retrieved as follows:

$$\varepsilon = \frac{jc}{2\pi f} \frac{1}{F_g l} \frac{1-\Gamma}{1+\Gamma} \ln(\Psi) \quad (16)$$

The coaxial-cage line is inserted in a cryostat and cooled using dry ice pellets. The measurements were performed first progressively decreasing the temperature from 298 K to 200 K and then allowing the system to slowly reach room temperature. Each cycle lasted about 50 h, 10 h for cooling and 40 h for heating the sample. A Pt-100 probe was inserted in the coaxial-cage line to measure sample temperature during the entire cycle.

592 **Appendix D**

593 Supplementary material

594

595 **References**

596 Addison J. R., Electrical properties of saline ice at 1 kHz down to -150°C . *J. App. Phys.*, **46**(2),
597 513-522 (1975).

598 Bibring J.P., Y. Langevin, J.F. Mustard, F. Poulet, R. Arvidson, A. Gendrin, B. Gondet, N.
599 Mangold, P. Pinet, P. Forget, Global mineralogical and aqueous Mars history derived from
600 OMEGA/Mars Express data. *Science* **312**, 400–404 (2006).

601 Bierson C. J., S. Tulaczyk, S. W. Courville, N. E. Putzig, Strong MARSIS Radar Reflections
602 from the Base of Martian South Polar Cap may be due to Conductive Ice or Minerals.
603 *Geophysical Research Letters*, e2021GL093880 (2021).

604 Bishop J.L., A.G. Fairèn, J.R. Michalski, L. Gago-Duport, L.L. Baker, M. A. Velbel, C., Gross,
605 E.B. Rampe, Surface clay formation during short-term-warmer and wetter conditions on largely
606 cold ancient Mars. *Nature Astronomy* **2**, 206-2013 (2018).

607 Bittelli M., M. Flury, K. Roth Use of dielectric spectroscopy to estimate ice content in frozen
608 porous media. *Water resources research*, **40**(4) (2004).

609 Bristow T.F., E.B. Rampe, C.N. Achilles, D.F. Blake, S.J. Chipera, P. Craig, J.A. Crisp, D.J.
610 Des Marais, R.T. Downs, R. Gellert, J.P. Grotzinger, S. Gupta, R.M. Hazen, B. Horgan, J.V.
611 Hogancamp, P.R. Mahaffy, A.C. McAdam, D.W. Ming, J.M. Morookian, R.V. Morris, S.M.
612 Morris, A. H. Treiman, D.T. Vaniman, A.R. Vasavada, A.S. Yen, Clay Mineral Diversity and
613 Abundance in Sedimentary Rocks of Gale Crater, Mars. *Sci. Adv.* **4**, eaar3330 (2018).

614 Burton E. F., L. G. Turnbull, Dielectric constants of solids at high frequencies and the influence
615 of water of crystallization on dielectric constant. Proceedings of the Royal Society of London.
616 Series A-Mathematical and Physical Sciences, 158(893), 182-198 (1937).

617 Cadène A., B. Rotenberg, S. Durand-Vidal, J. C. Badot, P. Turq, Dielectric spectroscopy as a
618 probe for dynamic properties of compacted smectites. *Physics and Chemistry of the Earth, Parts*
619 *A/B/C*, **31**(10-14), 505-510 (2006).

620 Chelidze T. L., Y. Gueguen, C. Ruffet, Electrical spectroscopy of porous rocks: a review—II.
621 Experimental results and interpretation. *Geophysical Journal International*, **137**(1), 16-34
622 (1999).

623 Cheng C. K., The dielectric constants of some metallic sulphates containing various amounts of
624 water of crystallization. *The London, Edinburgh, and Dublin Philosophical Magazine and*
625 *Journal of Science*, **30**(203), 505-515 (1940).

626 Chevrier V. F., J. Hanley, T. S. Altheide, Stability of perchlorate hydrates and their liquid
627 solutions at the Phoenix landing site, Mars. *Geophys. Res. Lett.*, **36**(10) (2009).

628 Clark B.C., R.E. Arvidson, R. Gellert, R.V. Morris, D.W. Ming, L. Richter, S.W. Ruff, J.R.
629 Michalski, W.H. Ferrand, A. Yen, K.E. Herkenhoff, R. Li, S.W. Squyres, C. Schröder, G.
630 Klingelhöfer, J.F. Bell III, Evidence for montmorillonite or its compositional equivalent in
631 Columbia Hills, Mars. *J. Geophys. Res.* **112**, E06S01 (2007).

632 Cunje A. B., R. R. Ghent, A. Boivin, C. A. Tsai, D. Hickson, Dielectric properties of Martian
633 regolith analogs and smectite clays. In Lunar and Planetary Science Conference (No. **2083**, p.
634 1805) (2018).

635 Ehlmann B. L., J. F. Mustard, S. L. Murchie, J.P. Bibring, A. Meunier, A. Fraeman, Y. Langevin,
636 Subsurface water and clay mineral formation during the early history of Mars, *Nature* **479**,53–
637 60 (2011).

638 Ehlmann B. L., J.F. Mustard, G.A. Swayze, R.N. Clark, J.L. Bishop, F. Poulet, D.J. Des Marais,
639 L. H. Roach, R. E. Milliken, J.J. Wray, O. Barnouin-Jha, S.L. Murchie, Identification of hydrated
640 silicate minerals on Mars using MRO-CRISM: Geologic context near Nili Fossae and
641 implications for aqueous alteration. *Journal of Geophysical Research* **114**, E00D08, (2009).

642 Ehlmann B.L., C.S. Edwards, Mineralogy of the Martian surface. *Annu Rev Earth Planet Sci* **42**,
643 291-315 (2014).

644 Ehlmann B.L., G. Berger, N. Mangold, J.R. Michalski, D.C. Catling, S.V. Ruff, E. Chassefière,
645 P.B. Niles, V. Chevrier, F. Poulet, Geochemical consequences of widespread clay mineral
646 formation in Mars' Ancient Crust. *Space Science Review* **174**, 329–364 (2013).

647 Fujino K., Electrical properties of sea ice. *Phys. of Snow and Ice: proc.* **1**(1), 633-648 (1967).

648 Gaudin A., E. Dehouck, O. Grauby, N. Mangold, Formation of clay minerals on Mars: Insights
649 from long-term experimental weathering of olivine. *Icarus*, **311**, 210-223 (2018).

650 Gooding J.L., D.W. Muenow, Martian volatiles in shergottite EETA 79001: New evidence from
651 oxidized sulfur and sulfur-rich aluminosilicates. *GCA* **50**(6), 1049-1059 (1986).

652 Grima C., J. S. Greenbaum, E. J. Lopez Garcia, K. M. Soderlund, A. Rosales, D. D. Blankenship,
653 D. A. Young, Radar detection of the brine extent at McMurdo Ice Shelf, Antarctica, and its
654 control by snow accumulation. *Geophysical Research Letters*, **43**(13), 7011-7018 (2016).

655 Grimm R. E., D. E. Stillman, S. F. Dec, M. A. Bullock, Low-frequency electrical properties of
656 polycrystalline saline ice and salt hydrates. *J. Phys. Chem. B* **112**(48), 15382-15390 (2008).

657 Gross G.W., P.M. Wong, K. Humes, Concentration dependent solute redistribution at the ice-
658 water phase boundary. III. Spontaneous convection. Chloride solutions. *J. Chem. Phys.* **67**(11),
659 5264–5274 (1977).

660 Ishida T., Dielectric Behavior of Clay Surfaces. *Encyclopedia of Surface and Colloid, Science*,
661 1385-1392 (2002).

662 Johnston C. T., Probing the nanoscale architecture of clay minerals. *Clay Minerals*, **45**(3), 245-
663 279 (2010).

664 Kaatze U., Complex permittivity of water as a function of frequency and temperature. *J. Chem.*
665 *Engin. Data* **34**(4), 371-374 (1989).

666 Kaden H., F. Königer, M. Strømme, G. A. Niklasson, K. Emmerich, Low-frequency dielectric
667 properties of three bentonites at different adsorbed water states. *Journal of colloid and interface*
668 *science*, **411**, 16-26 (2013).

669 Kamiyoshi K. I., T. Miyamoto, Dielectric properties of the water of crystallization. In *Science*
670 *Reports of the Research Institutes, Tohoku University. Ser. A, Physics, Chemistry and*
671 *Metallurgy, Vol. 2, pp. 370-379, (1950).*

672 Kao K. C., Dielectric phenomena in solids. Elsevier (2004).

673 Kaviratna P. D., T. J. Pinnavaia, P. A. Schroeder, Dielectric properties of smectite clays. *Journal*
674 *of Physics and Chemistry of Solids*, **57**(12), 1897-1906 (1996).

675 Kounaves S.P., B.L. Carrier, G.D. O'Neil, S.T. Stroble, M.W. Claire Evidence of martian
676 perchlorate, chlorate, and nitrate in Mars meteorite EETA79001: Implications for oxidants and
677 organics. *Icarus* **229**, 206-213 (2014).

678 Kułacz K., J. Waliszewski, S. Bai, L. Ren, H. Niu, K. Orzechowski, Changes in structural and
679 dielectric properties of nontronite caused by heating. *Applied Clay Science*, **202**, 105952 (2021).

680 Kułacz K., K. Orzechowski, Nontronite and intercalated nontronite as effective and cheap
681 absorbers of electromagnetic radiation. *Dalton Transactions*, **48**(12), 3874-3882 (2019).

682 Kuligiewicz A., A. Derkowski, Tightly bound water in smectites. *American Mineralogist*,
683 **102**(5), 1073-1090 (2017).

684 Lauro S. E., E. Pettinelli, G. Caprarelli, L. Guallini, A. P. Rossi, E. Mattei, R. Orosei, Multiple
685 subglacial water bodies below the south pole of Mars unveiled by new MARSIS data. *Nat.*
686 *Astron.*, **5**(1), 63-70 (2021).

687 Leshin L.A., E. Vicenzi, Aqueous processes recorded by Martian meteorites: Analyzing Martian
688 water on Earth. *Elements* **2**(3), 157-162 (2006).

689 Liu N., J. K. Mitchell, Modelling electromagnetic properties of saturated sand and clay.
690 *Geomechanics and Geoengineering: An International Journal*, **4**(4), 253-269 (2009).

691 Lorek A., N. Wagner, Supercooled interfacial water in fine-grained soils probed by dielectric
692 spectroscopy. *The Cryosphere*, **7**(6), 1839-1855 (2013).

693 Mattei E., S. E. Lauro, E. Pettinelli, G. Vannaroni, Coaxial-Cage Transmission Line for
694 Electromagnetic Parameters Estimation. *IEEE Trans. Instr. Meas.* **62**, (2013).

695 Mattei E., S. E. Lauro, G. Vannaroni, B. Cosciotti, F. Bella, E. Pettinelli, Dielectric
696 measurements and radar attenuation estimation of ice/basalt sand mixtures as martian Polar Caps
697 analogues. *Icarus* **229**, 428-433 (2014).

698 McSween H.Y., What we have learned about Mars from SNC meteorites. *Meteoritics* **29**, 757-
699 779 (1994).

700 Moore J. C., N. Maeno, Dielectric properties of frozen clay and silt soils. *Cold regions science
701 and technology*, **21**(3), 265-273 (1993).

702 Murchie S.L., J.F. Mustard, B.L. Ehlmann, R.E. Milliken, J.L. Bishop, N.K. McKeown, D.J.
703 Noe Dobrea EZ, F.P. Seelos, D.L. Buczkowski, S.M. Wiseman, R.E. Arvidson, J.J. Wray, G.
704 Swayze, R.N. Clark, Des Marais, A.S. McEwen, J.P. Bibring, A synthesis of Martian aqueous
705 mineralogy after 1 Mars year of observations from the Mars Reconnaissance Orbiter. *J Geophys
706 Res Planets* **114**, E00D06 (2009).

707 Murchie S.L., R. Arvidson, P. Bedini, K. Beisser, J.P. Bibring, J. Bishop, J. Boldt, P. Cavender,
708 , T. Choo, R.T. Clancy, E.H. Darlington, D. Des Marais, R. Espiritu, D. Fort, R. Green, E.
709 Guinness, J. Hayes, C. Hash, K. Heffernan, J. Hemmler, G. Heyler, D. Humm, J. Hutchison, N.
710 Izenberg, R. Lee, J. Lees, D. Lohr, E. Malaret, T. Martin, J.A. McGovern, P. McGuire, R. Morris,
711 J. Mustard, S. Pelkey, E. Rhodes, V. Robinson, T. Roush, E. Schaefer, G. Seagrave, F. Seelos,
712 P. Silverglate, S. Slavney, M. Smith, W. J. Shyong, K. Strohbahn, H. Taylor, P. Thompson, B.
713 Tossman, M. Wirzburger, M. Wolff, Compact Reconnaissance Imaging Spectrometer for Mars
714 (CRISM) on Mars Reconnaissance Orbiter (MRO). *J. Geophys. Res.* **112**, E05S03 (2007).

715 Mustard J.F., C.D. Cooper, M.K. Rifkin, Evidence for recent climate change on Mars from the
716 identification of youthful near-surface ground ice. *Nature* **412**, 411-414 (2001).

717 Muttik N., F.M. McCubbin, L.P. Keller, A.R. Santos, W.A. McCutcheon, P.P. Provencio, Z.
718 Rahman, C.K. Shearer, J.W. Boyce, C.B. Agee Inventory of H₂O in the ancient Martian regolith
719 from Northwestern Africa 7034: The important role of Fe oxides. *Geophys Res Lett.* **41**(23),
720 8235-8244 (2014).

721 Nair C. R., V. Unnikrishnan, Stability of the Liquid Water Phase on Mars: A Thermodynamic
722 Analysis Considering Martian Atmospheric Conditions and Perchlorate Brine Solutions. *ACS
723 omega* **5**(16), 9391-9397 (2020).

724 Nicolson A. M., G. F. Ross, Measurement of the intrinsic properties of materials by time-domain
725 techniques. *IEEE Trans. Instr. Meas.* **19**(4), 377-382 (1970).

726 Nobes D. C., E. F. Davis, S. A. Arcone, “Mirror-image” multiples in ground-penetrating radar.
727 *Geophysics*, **70**(1), K20-K22 (2005).

728 Olhoeft G. R., Electrical properties of natural clay permafrost. *Canadian Journal of Earth*
729 *Sciences*, **14**(1), 16-24 (1977).

730 Olhoeft G. R., Electrical properties of rocks. *Physical properties of rocks and minerals*, **2**, 257-
731 297 (1981).

732 Olhoeft G. R., Tables of room temperature electrical properties for selected rocks and minerals
733 with dielectric permittivity statistics. US Department of the Interior, *Geological Survey* (1979).

734 Orosei R., S. E. Lauro, E. Pettinelli, A. Cicchetti, M. Coradini, B. Cosciotti, R. Seu, Radar
735 evidence of subglacial liquid water on Mars. *Science*, **361**(6401), 490-493 (2018).

736 Parkhomenko E. I., *Electrical Properties of Rocks* (1967).

737 Pettinelli E., S. E. Lauro, B. Cosciotti, E. Mattei, F. Di Paolo, G. Vannaroni, Dielectric
738 characterization of ice/MgSO₄·11H₂O mixtures as Jovian icy moon crust analogues. *Earth and*
739 *Planetary Science Letters*, **439**, 11-17 (2016).

740 Plesa A.C., S. Padovan, N. Tosi, D. Breuer, M. Grott, M.A. Wieczorek, T. Spohn, S.E. Smrekar,
741 W.B. Banerdt, The thermal state and interior structure of Mars. *Geophys. Res. Lett.* **45**, 12198-
742 12209, (2018).

743 Poulet F., D. Mangold, D. Loizeau, J.P. Bibring, Y. Langevin, J. Michalski, B. Gondet,
744 Abundance of minerals in the phyllosilicate-rich units on Mars. *Astron. Astrophys* **487**, L41–
745 L44 (2008).

746 Primm K. M., D. E. Stillman, T. I. Michaels, Investigating the hysteretic behavior of Mars-
747 relevant chlorides. *Icarus* **342**, 113342 (2020).

748 Rampe E. B., D. W. Ming, D. F. Blake, T. F. Bristow, S. J. Chipera, J. P. Grotzinger, R. V.
749 Morris, S. M. Morrison, D. T. Vaniman, A. S. Yen, C. N. Achilles, P. I. Craig, D. J. Des Marais,
750 R. T. Downs, J. D. Farmer, K. V. Fendrich, R. Gellert, R. M. Hazen, L. C. Kah, J. M. Morookian,
751 T. S. Peretyazhko, P. Sarrazin, A. H. Treiman, J. A. Berger, J. Eigenbrode, A. G. Fairén, O.
752 Forni, S. Gupta, J. A. Hurowitz, N. L. Lanza, M. E. Schmidt, K. Siebach. B. Sutter, L. M.
753 Thompson, Mineralogy of an ancient lacustrine mudstone succession from the Murray
754 formation, Gale crater, Mars. *Earth and Plan. Science Lett.* **471**, 172-185 (2017).

755 Rampe E. B., D.F. Blake, T.F. Bristow, D.W. Ming, D.T. Vaniman, R.V. Morris, C.N. Achilles,
756 S.J. Chipera, S.M. Morrison, V.M. Tu, A.S. Yen, N. Castle, G.W. Downs, R.T. Downs, J.P.
757 Grotzinger, R.M. Hazen, A.H. Treiman, T.S. Peretyazhko, D.J. Des Marais, R.C. Walroth, P.I.
758 Craig, J.A. Crisp, B. Lafuente, J.M. Morookian, P.C. Sarrazin, M.T. Thorpe, J.C. Bridges, L.A.
759 Edgar, C.M. Fedo, C. Freissinet, R. Gellert, P.R. Mahaffy, H.E. Newsom, J.R. Johnson, L.C.

760 Kah, K.L. Siebach, J. Schieber, V.Z. Sun, A.R. Vasavada, D. Wellington, R.C. Wiens,
761 Mineralogy and geochemistry of sedimentary rocks and eolian sediments in Gale crater, Mars:
762 A review after six Earth years of exploration with Curiosity. *Geochemistry* **80**, 125605 (2020a).
763 Rampe E. B., T. F. Bristow, R. V. Morris, S. M. Morrison, C. N. Achilles, D. W. Ming, D. T.
764 Vaniman, D. F. Blake, V. M. Tu, S. J. Chipera, A. S. Yen, T. S. Peretyazhko, R. T. Downs, R.
765 M. Hazen, A. H. Treiman, J. P. Grotzinger, N. Castle, P. I. Craig, D. J. Des Marais, M. T. Thorpe,
766 R. C. Walroth, G. W. Downs, A. A. Fraeman, K. L. Siebach, R. Gellert, A. C. McAdam, P. -Y.
767 Meslin, B. Sutter, M. R. Salvatore, Mineralogy of Vera Rubin Ridge from the Mars Science
768 Laboratory CheMin Instrument. *J. Geophys. Res.* **125**, e2019JE006306. (2020b).
769 Rutishauser A., D. D. Blankenship, M. Sharp, M. L. Skidmore, J. S. Greenbaum, C. Grima, D.
770 A. Young, Discovery of a hypersaline subglacial lake complex beneath Devon Ice Cap, Canadian
771 Arctic. *Science advances*, **4**(4), eaar4353 (2018).
772 Saarenketo T., Electrical properties of water in clay and silty soils. *Journal of applied*
773 *geophysics*, **40**(1-3), 73-88 (1998).
774 Saltas V., F. Vallianatos, D. Triantis, Dielectric properties of non-swelling bentonite: The effect
775 of temperature and water saturation. *Journal of Non-Crystalline Solids*, **354**(52-54), 5533-
776 5541(2008).
777 Siegert M. J., A 60-year international history of Antarctic subglacial lake exploration. *J. Geol.*
778 *Soc. Lond. Mem.* **461**, 7–21 (2018).
779 Sihvola A. H., Electromagnetic mixing formulas and applications (No. 47). Iet. (1999).
780 Smith I. B., D. Lalich, C. Rezza, B. Horgan, J. L. Whitten, S. Nerozzi, J. W. Holt, A Solid
781 Interpretation of Bright Radar Reflectors Under the Mars South Polar Ice. *Geophysical Research*
782 *Letters*, e2021GL093618 (2021).
783 Sori M. M., A. M. Bramson, Water on Mars, with a grain of salt: local heat anomalies are
784 required for basal melting of ice at the south pole today. *Geophys. Res. Lett.* **46**(3), 1222-1231
785 (2019).
786 Sposito G., R. Prost, Structure of water adsorbed on smectites. *Chemical Reviews*, **82**(6), 553-
787 573 (1982).
788 Stewart R. D., R. R. Unterberger, Seeing through rock salt with radar. *Geophysics*, **41**(1), 123-
789 132, (1976).
790 Stillman D. E., J. A. MacGregor, R. E. Grimm, Electrical response of ammonium-rich water ice.
791 *Ann. Glaciol.* **54**(64), 21–26 (2013).
792 Stillman D. E., R. E. Grimm, Radar penetrates only the youngest geological units on Mars. *J.*
793 *Geophys. Res. Plan.* **116**(E3) (2011a).

794 Stillman D. E., R. E. Grimm, S. F. Dec, Low-Frequency Electrical Properties of Ice– Silicate
795 Mixtures. *J. Phys. Chem. B* **114**(18), 6065-6073 (2010).

796 Stillman D. E., R. E. Grimm. Dielectric signatures of adsorbed and salty liquid water at the
797 Phoenix landing site, Mars. *J. Geophys. Res. Plan.* **116**(E9) (2011b)

798 Stillman D., G. Olhoeft, Frequency and temperature dependence in electromagnetic properties
799 of Martian analog minerals. *Journal of Geophysical Research: Planets*, **113**(E9), (2008).

800 Stillman, D. E., Pettinelli, E., Primm, K. M., Caprarelli, G., Mattei, E., Lauro, S. E., & Cosciotti,
801 B. Perchlorate and Chloride Brines as the Cause of the MARSIS Bright Basal Reflections:
802 Laboratory Measurements. *LPI Contributions*, 2614, 6028, (2021).

803 Tangari A. C., L. Marinangeli, F. Scarciglia, L. Pompilio, E. Piluso, Volcanic holocrystalline
804 bedrock and hydrothermal alteration: a terrestrial analogue for Mars. *Minerals*, **10**(12), 1082
805 (2020).

806 Thomas N. H., B. L. Ehlmann, W. Rapin, F. Rivera-Hernández, N. T. Stein, J. Frydenvang, R.
807 C. Wiens, Hydrogen Variability in the Murray Formation, Gale Crater, Mars. *Journal of*
808 *Geophysical Research: Planets*, **125**(9), e2019JE006289 (2020).

809 Toner J. D., D. C. Catling, Chlorate brines on Mars: implications for the occurrence of liquid
810 water and deliquescence. *Earth Planet. Sci. Lett.* **497**, 161–168 (2018).

811 Toner J.D., D.C. Catling, B. Light, The formation of supercooled brines, viscous liquids, and
812 low-temperature perchlorate glasses in aqueous solutions relevant to Mars. *Icarus* **233**, 36-47
813 (2014).

814 Treiman A. H., D. L. Bish, D. T. Vaniman, S. J. Chipera, D. F. Blake, D. W. Ming, R. V. Morris,
815 T. F. Bristow, S. M. Morrison, M. B. Baker, E. B. Rampe, R. T. Downs, J. Filiberto, A. F.
816 Glazner, R. Gellert, L. M. Thompson, M. E. Schmidt, L. Le Deit, R. C. Wiens, A. C. McAdam,
817 C. N. Achilles, K. S. Edgett, J. D. Farmer, K. V. Fendrich, J. P. Grotzinger, S. Gupta, J. M.
818 Morookian, M. E. Newcombe, M. S. Rice, J. G. Spray, E. M. Stolper, D. Y. Sumner, A. R.
819 Vasavada, A. S. Yen, Mineralogy, provenance, and diagenesis of a potassic basaltic sandstone
820 on Mars: CheMin X-ray diffraction of the Windjana sample (Kimberley area, Gale crater). *J.*
821 *Geophys. Res. Planets* **121**, 75–106 (2016).

822 Treiman A.H., R.A. Barrett, J.L., Gooding, Preterrestrial aqueous alteration of the Lafayette
823 (SNC) meteorite. *Meteoritics* **28**(1), 86-97(1993).

824 Tulaczyk S. M., N. T. Foley, The role of electrical conductivity in radar wave reflection from
825 glacier beds. *The Cryosphere*, **14**(12), 4495-4506 (2020).

826 Weir W. B., Automatic measurement of complex dielectric constant and permeability at
827 microwave frequencies. *Proc. IEEE* **62**-1, 33–36 (1974).

828 Wersin P., E. Curti, C. A. J. Appelo, Modelling bentonite–water interactions at high solid/liquid
829 ratios: swelling and diffuse double layer effects. *Applied Clay Science*, **26**(1-4), 249-257 (2004).

830 Wieczorek M.A., Constraints on the composition of the martian south polar cap from gravity
831 and topography. *Icarus* **196**, 506-517 (2008).

832 Young K. F., H. P. R. Frederikse, Compilation of the static dielectric constant of inorganic solids.
833 *Journal of Physical and Chemical Reference Data*, **2**(2), 313-410 (1973).

834 835 **Acknowledgments**

836 The authors would like to thank Prof. Orzechowski for the use of his dataset on real and imaginary
837 parts of natural nontronite, and Dr. Antonio Baliva and Dr. Luca Colantuono for collecting and
838 preparing clay samples measured in this work. This work was supported by the Italian Space
839 Agency (ASI) through contract ASI-INAF 2019–21-HH.0.

840